

Generation of Radially Polarized Single Photons with Plasmonic Bullseye Antennas

Danylo Komisar,* Shailesh Kumar, Yinhui Kan, Cuo Wu, and Sergey I. Bozhevolnyi

Cite This: *ACS Photonics* 2021, 8, 2190–2196

Read Online

ACCESS |



Metrics & More



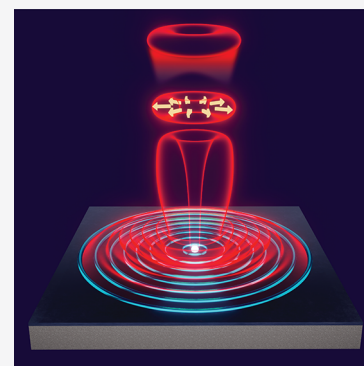
Article Recommendations



Supporting Information

ABSTRACT: Radially polarized optical beams are desirable in many applications because of their property to generate longitudinally polarized fields when being strongly focused. Single-photon sources are however normally limited to the generation of linearly polarized photons due to their dipolar nature. Here, we report on emission of radially polarized single photons from a nitrogen-vacancy (NV) center in a nanodiamond (ND) coupled to a bull's-eye plasmonic antenna. Design optimization and characterization of plasmonic bull's-eye antennas consisting of polymer circular nanoridges deterministically fabricated on a silica protected silver film around an NV-ND emitter are reported. We demonstrate with numerical simulations that the collection efficiency for photons emitted at the design wavelength can exceed 80% with optimized bull's-eye structures. Analysis of the emission angular distribution indicates that, even when limiting the detection to the main lobe by using an 0.2 NA objective, the detection efficiency can overreach 55%. A 3-fold enhancement in the total number of detected radially polarized photons is experimentally observed with an NV-ND single-photon emitter being coupled to a bull's-eye antenna. Generation of radially polarized single photons suggests new interesting possibilities for single-photon imaging and sensing.

KEYWORDS: single photon, bull's-eye, radial polarization, plasmonics, collection efficiency, nitrogen-vacancy center

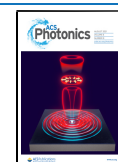


Radially polarized light beams are used for subdiffraction imaging,^{1,2} noise-proof optical communication,^{3,4} quantum key distribution,⁵ and other applications.⁶ Single-photon beams with radial polarization are desired in the rapidly developing quantum communication, quantum information processing, and metrology.^{7–11} Quantum technology requires single-photon sources with high photon rate, high collection efficiency (CE), well-defined polarization states, and on-demand photon generation. To make sources feasible for large scale fabrication, the room-temperature operation and on-chip integration requirements should be fulfilled.¹² Single photons are produced by a variety of emitters such as isolated atoms, ions, molecules, quantum dots, or defect centers in crystals.^{13–16} Nanodiamonds containing nitrogen-vacancy (NV-ND) centers are effective for room temperature single-photon generation.^{17,18} However, the photons are emitted in all directions and are not polarized. There are three main challenges in obtaining efficient single-photon sources: first, to increase the photon generation rate of a quantum emitter (QE); second, to control the polarization of emission; and third, to collect all the emitted photons from QE. The photon emission rate of NV-NDs can be enhanced by coupling NV-NDs to dielectric or plasmonic structures,^{19–30} as well as the beam properties can be controlled by fabricating a suitable environment for the emitter.^{31,32} The polarization of emission can be controlled by coupling NV-NDs to waveguides or localized plasmon modes followed by outcoupling with antennas to far-field.^{27,33,34} The control of the outcoupler

design allows the generation of single photons with a predefined polarization state, far-field intensity, and phase distributions. Generation of linearly²⁷ and circularly polarized single-photon beams³⁵ from NV-NDs has been demonstrated. Previously, an outcoupling grating was utilized for achieving efficient collection from multiple NV centers.³⁶ Here, we demonstrate the generation of radially polarized single photons by coupling NV-NDs to the plasmonic bull's-eye antenna. We have optimized the structure to obtain high CE by numerical simulations. We fabricated the structure by utilizing a positioning technique that we have used before.^{35,37,38} With the optimized structure, we obtain a 3 times increase in the number of photons collected after fabrication of the bull's-eye structure compared to emission from an NV-ND on a bare substrate. We estimate a CE of $\sim 74\%$, for an objective of 0.9 numerical aperture (NA). Collection efficiency is defined as a ratio of power collected by the objective in the far-field over total power generated by a dipole in the presence of the plasmonic structure.

Received: March 26, 2021

Published: July 9, 2021



A schematic of the experiment is presented in Figures 1 and 2(a). The nanodiamond containing a single NV-center with

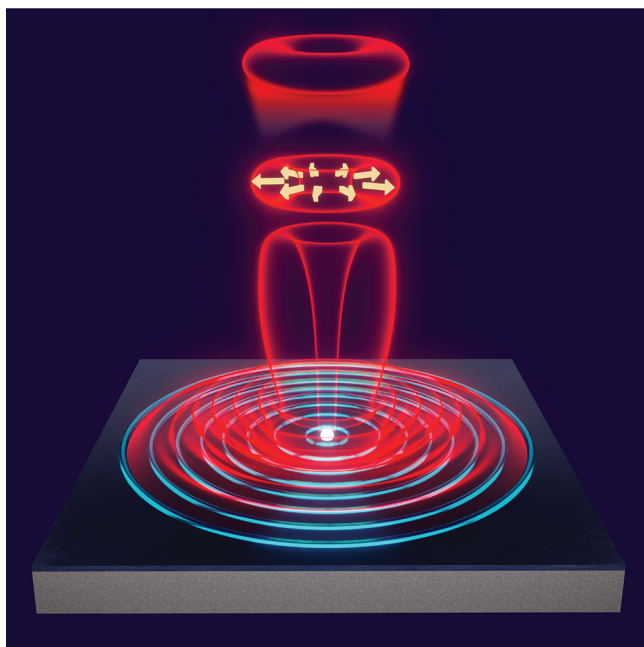


Figure 1. Operation of the radially polarized single-photon source. The excited QE with normal to surface dipole moment generates SPP waves on the air/metal interface. SPP scatters on concentric dielectric periodic ridges (blue), resulting in upward emission with a doughnut-shaped intensity profile. Arrows represent radial polarization of the single-photon beam.

vertical dipole orientation is placed on the silica-coated Ag surface. The SiO₂ spacer between NV-ND and Ag is used to avoid the quenching of emission. The NV-ND is surrounded

by several concentric dielectric ridges, so-termed bull's-eye grating. The excited NV-center spontaneously decays and generates surface plasmon polaritons (SPPs) on the Ag/SiO₂/Air interface. SPPs propagate away from the NV-ND and are subsequently scattered by the bull's-eye grating. The ridges' spacing and size are adjusted to match the second-order Bragg resonance to enhance the SPP scattering. Scattered light interferes constructively in the far-field, forming the collimated doughnut-shaped radially polarized outgoing beam. The radial polarization of the beam and the doughnut-shape are defined by the rotational symmetry of the device. We have designed our device to radiate at an angle close to the plane normal. We note that beams propagating at large angles with respect to the surface normal and beams directed at several angles simultaneously can be constructed by choosing the proper structure period and duty cycle of the bull's-eye antenna [see the Supporting Information (SI)].

In the following, we first describe plasmonic bull's-eye antenna structure optimization by numerical simulation followed by theoretical analysis of bull's-eye antenna performance. Subsequently, we present details of our experiment, followed by a discussion of the results obtained.

We calculated optimal parameters for the bull's-eye structure by looking for the highest CE while varying the structure geometry in COMSOL Multiphysics. The NV center is represented by a vertically oriented electric dipole emitting light at a wavelength of $\lambda_0 = 670$ nm. The dipole is surrounded by 12 circular scattering ridges of 180 nm thick hydrogen silsesquioxane (HSQ). The dipole is positioned 50 nm above the substrate. The substrate is composed of an optically thick 100 nm Ag layer covered with a 20 nm SiO₂ spacer. Optical constants for silver and SiO₂ were taken from Johnson et al.³⁹ and Malitson,⁴⁰ respectively. The refractive index of HSQ was set to 1.41.⁴¹

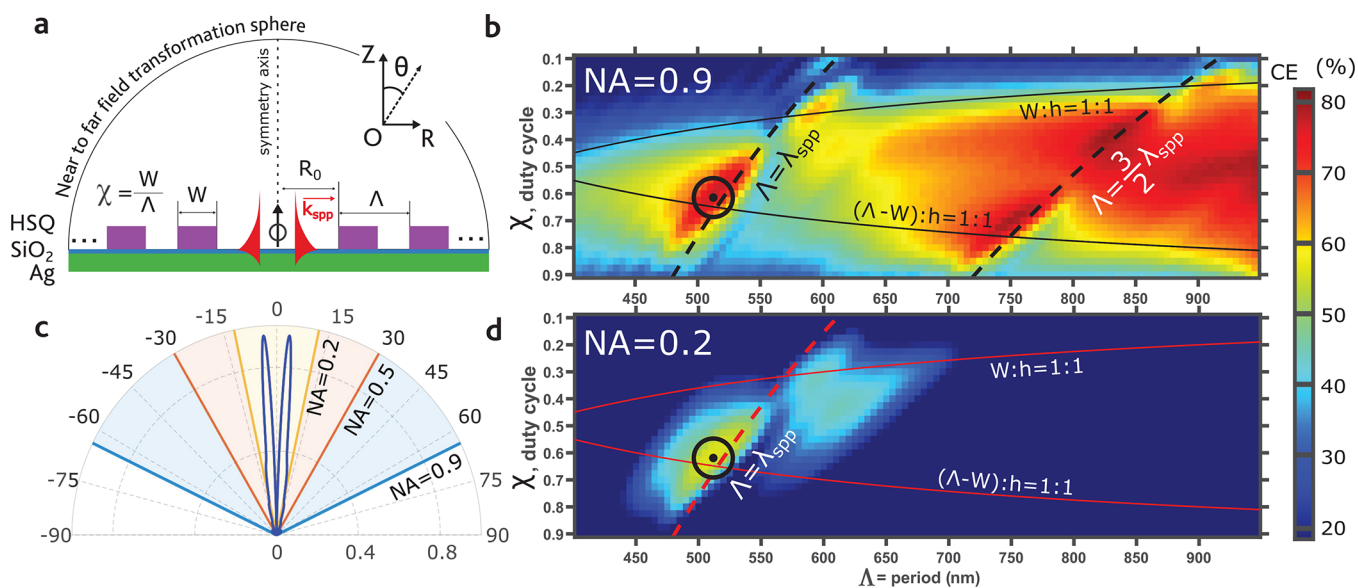


Figure 2. (a) Cross section of the circular plasmonic structure: vertical dipole on the symmetry axis generates SPPs, which scatters on periodical HSQ ridges. Emission is calculated using near-to-far field transformation on the semispherical boundary enclosing the structure. (b) and (d) Maps of collection efficiency over the structure period and duty cycle calculated for collection angles 64° (NA = 0.9) and 12° (NA = 0.2). Black dot: $\Lambda = 516$ nm, $\chi = 0.61$ corresponds to the maximum of CE. Dashed curves depict Bragg resonances (eq 2). The region of (Λ, χ) parameters feasible for e-beam lithography implementation is limited by the 1:1 structure aspect ratio and lies between solid lines. (c) Far-field angular distribution of emission of bull's-eye structure calculated for the optimal set of parameters for $\Lambda = 516$ nm, $W = 315$ nm, $\chi = 0.61$, and $R_0 = 520$ nm.

The NV-center radiation transition is associated with two dipolar contributions that are perpendicular to each other.^{42,43} In general, the transition dipoles have projections both in the vertical (\vec{d}_z) and horizontal (\vec{d}_r) directions. Previous studies of the electric dipole emission placed in the proximity to the silver film^{44–46} show several reasons to utilize only the vertical dipole component for our purpose.³⁶ First, the radiative decay rate enhancement is observed only for the vertical orientation of the dipole, because the horizontal dipole radiation is suppressed by that of the mirrored antiphase dipole in the silver film. Moreover, the coupling of vertical dipole radiation into SPPs, in comparison to that of horizontal dipole radiation, is considerably higher. Thus, we neglect a weak horizontal dipole contribution and consider only the dominating vertical dipole contribution in our study. In the experiment, we ensure the presence of a strong out-of-plane dipole component of the NV center in the investigated nanodiamonds by selecting those that strongly luminesce when being illuminated with a tightly focused radially polarized laser beam, which produces a strong vertical electric field component of the pump beam in the focal plane.

The CE maps obtained for high and low NA objectives by varying the bull's-eye structure period and duty cycle are presented in Figure 2(b) and (d), respectively. The calculation is done for inner ridge radius $R_0 = 520$ nm. The structure with period $\Lambda = 516$ nm and duty cycle $\chi = 0.61$ has the highest CE = 74% for NA = 0.9 objective. Emitted light (56%) can be collected by low NA (0.2) objective. The corresponding set of grating parameters was chosen for experimental verification and is marked on the map by a black dot. The generated power density flow from the optimized structure is shown in Figure 3(c). The same level of CE ($\approx 80\%$) with NA = 0.9 objective

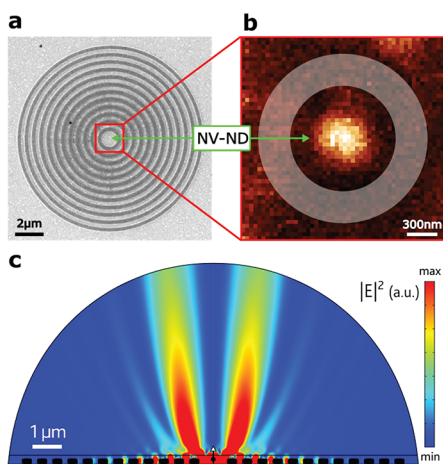


Figure 3. (a) Image of the bull's-eye structure. (b) Fluorescence scan of $2 \times 2 \mu\text{m}^2$ central area including NV-ND and the first HSQ ridge shown as a white circle. (c) On resonance power density flow from the optimized plasmonic antenna.

can be reached by utilizing first $\Lambda = \lambda_{\text{spp}}$ or second $\Lambda = 3\lambda_{\text{spp}}/2$ resonant regions marked by dashed lines on the map. However, the second resonant region of CE maximum corresponds to an outcoupled beam with emission angle $\theta_{\text{max}} = 24^\circ$ and, therefore, is not chosen for experimental investigations. The ridge aspect ratio $W:H(\text{HSQ}) = 0:55$ of the marked spot is convenient for the e-beam lithography procedure. A detailed description of the optimization procedure of dipole separation from the substrate, number of

ridges, inner ridge radius (R_0), and electromagnetic field distribution profiles in the grating can be found in the SI.

The direction of outcoming emission θ with respect to the surface normal is defined from the phase-matching condition

$$k_0 \sin(\theta) = k_{\text{spp}} \pm NG \quad (1)$$

where $k_{\text{spp}} = k_0 N_{\text{eff}}$ – SPP is the propagation constant, and $k_0 = 2\pi/\lambda_0$ is the wave vector of the free propagating wave. $G = 2\pi/\Lambda$, where Λ is the grating period. λ_0 is the wavelength of scattered light in vacuum, λ_{spp} is the wavelength of propagating SPP, and N is the grating order. $N_{\text{eff}} = (1 - \chi)N_{\text{eff}}(\text{air}) + \chi N_{\text{eff}}(\text{HSQ})$ is the effective refractive index of the grating. $\chi = W/\Lambda$ is the duty cycle. $N_{\text{eff}} = 1.29$ for the optimized bull's-eye antenna, with $N_{\text{eff}}(\text{air}) = 1.06$ and $N_{\text{eff}}(\text{HSQ}) = 1.44$. The calculation procedure for N_{eff} is described in Kan et al.³⁵

The efficiency of the outcoupling depends on the amplitude of the local SPP field on the ridges. The field can be intensified by matching resonances of multiple scattering of the SPP induced by the periodic nature of dielectric ridges. The high order Bragg resonances in multiple scattering are described by the equation

$$\Lambda = n\lambda_{\text{spp}}/2, \quad \text{with } n = 2, 3, 4, \dots \quad (2)$$

Matching the Bragg resonance condition increases the efficiency of the plasmonic antenna in two ways. First, the resonant back reflection from periodic ridges increases the Purcell factor (PF) and, therefore, the local field on the nanodiamond, which results in faster emission. Second, the enhanced local field on the ridges intensifies the scattering and positively influences the CE. SPP needs to travel fewer periods to be completely scattered upward. Therefore, ohmic losses have less effect. These two factors are illustrated in SI, Figure S7.

The high-CE resonant lines in Figure 2(b,d) correspond to Bragg resonances with orders $n = 2$ and $n = 3$ in eq 2. The case $n = 1$, i.e., the structure period $\Lambda = \lambda_{\text{spp}}/2$, corresponds to the total back reflection of the SPP, resulting in maximal enhancement of the PF. However, the SPP field amplitude on the ridges is minimal. The scattering process is not efficient, and a directional beam is not produced in the case of $n = 1$.

For the first resonant line, $n = 2$, $\Lambda = \lambda_{\text{spp}}$ and $\theta = 0^\circ$ defined from eq 1. The radially polarized beam has zero intensity along the surface normal ($\theta = 0^\circ$) because transverse field components cancel each other on the symmetry axis. Therefore, the emission maxima appear at a marginally larger angle, which we estimate from the numerical calculation. For example, for the $n = 2$ Bragg resonance, the angle $\theta_{\text{max}} = 5^\circ$, which is illustrated in Figure 2(c).

For the second resonant line, $n = 3$, $\Lambda = 3\lambda_{\text{spp}}/2$, and $\theta = 24^\circ$. For the third resonant line, $n = 4$, $\Lambda = 2\lambda_{\text{spp}}$, and $\theta = 40^\circ$. The Bragg resonances with $n > 4$ are not considered because of corresponding structure periods >800 nm, and therefore for 12 ridges, the structure radius $>10 \mu\text{m}$. At SPP propagation distances $>10 \mu\text{m}$, ohmic losses make SPP scattering inefficient. In our experiment, we utilized resonance with $n = 2$ and a corresponding $\Lambda = 516$ nm and a structure radius of $6 \mu\text{m}$. Investigated bull's-eye antenna is depicted in Figure 3. The field profiles and far-field angular distributions corresponding to $n = 2, 3, 4$ are presented in SI, Figure S7.

We note that even if Bragg resonance condition 2 is fulfilled, the scattered efficiency can be suppressed because of absorption of the SPP energy in metal under the ridges in

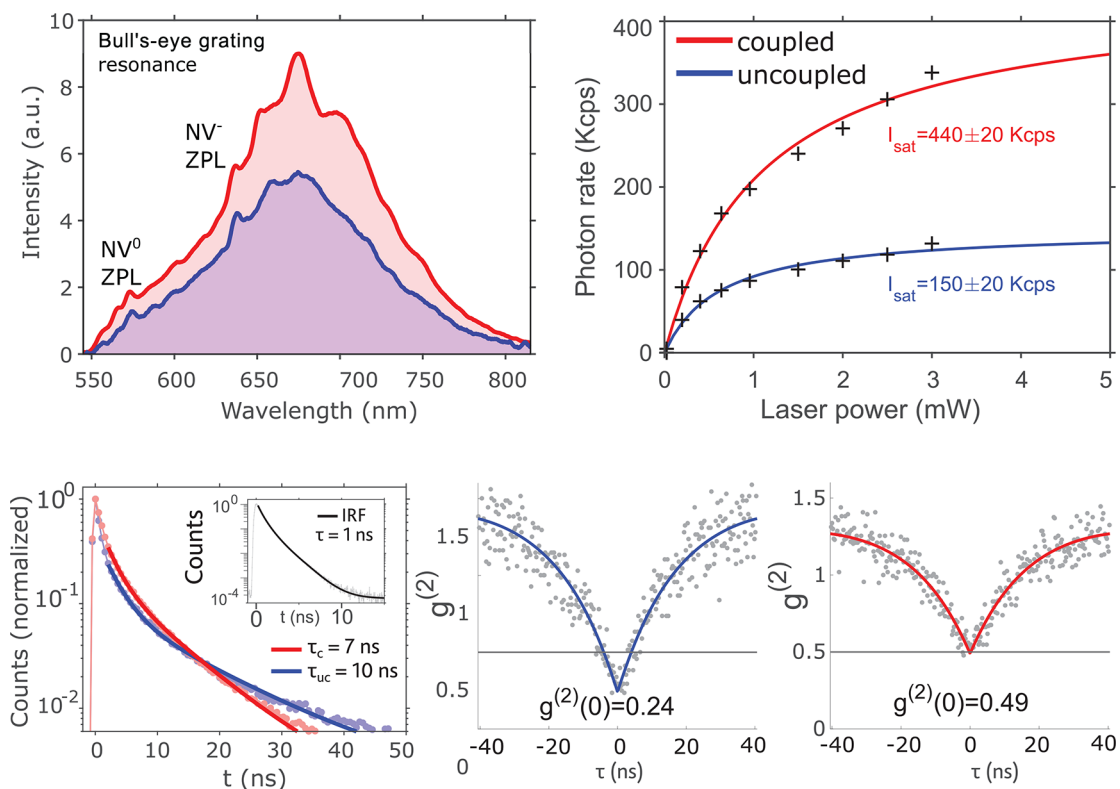


Figure 4. Characterization of the NV-ND before (blue) and after (red) coupling to bull's-eye grating under 532 nm CW optical excitation. (a) Emission spectra: NV⁰ ZPL at 575 nm, NV⁻ ZPL at 637 nm, and bull's-eye grating resonance at 670 nm peaks are present. (b) Saturation of the emission. (c) Fluorescence decay curves: raw data (points) and biexponential fit (solid lines). The inset shows the instrument response function (IRF). (d) and (e) Autocorrelation functions for uncoupled and coupled NV-ND.

the case of resonant back-forth multiple reflections of the SPP wave inside the ridge. That is the reason why CE along resonant dashed lines in Figure 2(b,d) is not uniformly maximal and drops around points $(\Lambda, \chi) = (560 \text{ nm}, 0.4)$ for the $\Lambda = \lambda_{\text{spp}}$ line and $(\Lambda, \chi) = [(800 \text{ nm}, 0.55); (800 \text{ nm}, 0.25)]$ for the $\Lambda = 3\lambda_{\text{spp}}/2$ line.

Having calculated the optimal parameters of the SPP outcoupler, we turn to the experiment description. First of all, we prepare the substrate. The 150 nm Ag layer is thermally evaporated on the Si wafer and covered with a protective 20 nm SiO₂ spacer using magnetron sputtering. The 3 nm Ti adhesive layer is deposited between Ag and SiO₂. Then, we fabricate golden alignment markers to make reference points for ND positioning and further alignment of bull's-eye structures around particles. Subsequently, we deposit NV-NDs by spin-coating of the ND solution. The NDs containing single color centers have a maximum size of ~ 100 nm.

To determine the NV-NDs positions, we take fluorescent maps under $\sim 200 \mu\text{W}$ of 532 nm CW laser excitation. Henceforward, we report the power of the laser beam before reaching the objective pupil. The power in the objective focal plane is diminished by factor six relatively to the presented values. Positions are determined relative to alignment markers at the corners of a $27 \times 27 \mu\text{m}^2$ area (SI, Figure S3). We search for NDs with predominantly normal to the surface dipole moment. We use a radially polarized excitation laser beam which produces substantial normal to the surface field component in the focal point and efficiently excites NV-NDs with a dominant dipole moment along the Z-axis. Then, we pick single-photon emitters by measuring autocorrelation and characterize their spectrum, lifetime, saturation curve, far-

field emission profile, and polarization properties. We perform all measurements at room temperature and use two $\lambda = 532$ nm lasers: a pulsed laser at 1 MHz for decay-rate measurements and a CW laser for other measurements. After precharacterization, we deposit HSQ bull's-eye structures around chosen NV-NDs using an e-beam negative resist lithography procedure. Figure 3(a),(b) shows a scanning electron microscope (SEM) image and a fluorescence scan image, respectively. Subsequently, to estimate the effect of coupling to the bull's-eye grating, we repeat all described characterization steps for the coupled emitter.

The fluorescence spectra of selected NV-ND before and after coupling to the bull's-eye antenna are presented in Figure 4(a). The fluorescence of NV-ND at room temperature has fwhm = 100 nm. The presence of zero phonon lines (ZPL) at 637 and 575 nm indicates that the charge state of NV in the ND flips between negative (NV⁻) and neutral (NV⁰). The peak around 670 nm is evidence of proper operation of the bull's-eye structure, which we optimized for $\lambda_0 = 670$ nm emission.

The photoluminescence decay curves for NV-ND emission before and after coupling are presented in Figure 4(c). The decay curves are fitted by the biexponential model $I = A_1 e^{-t/\tau_1} + A_2 e^{-t/\tau_2}$, where τ_1 and τ_2 are characteristic lifetimes of decay processes with amplitudes A_1 and A_2 , respectively. We attribute components of the double decay process to contributions from both NV⁰ and NV⁻ states with different lifetimes. The flipping between two states can be seen in the spectra depicted by two ZPLs in Figure 4(a). The average lifetime decreased from $\tau_{\text{uc}} = 10$ ns before coupling to $\tau_c = 7$ ns after coupling. We averaged lifetime components obtained from fitting using the equation

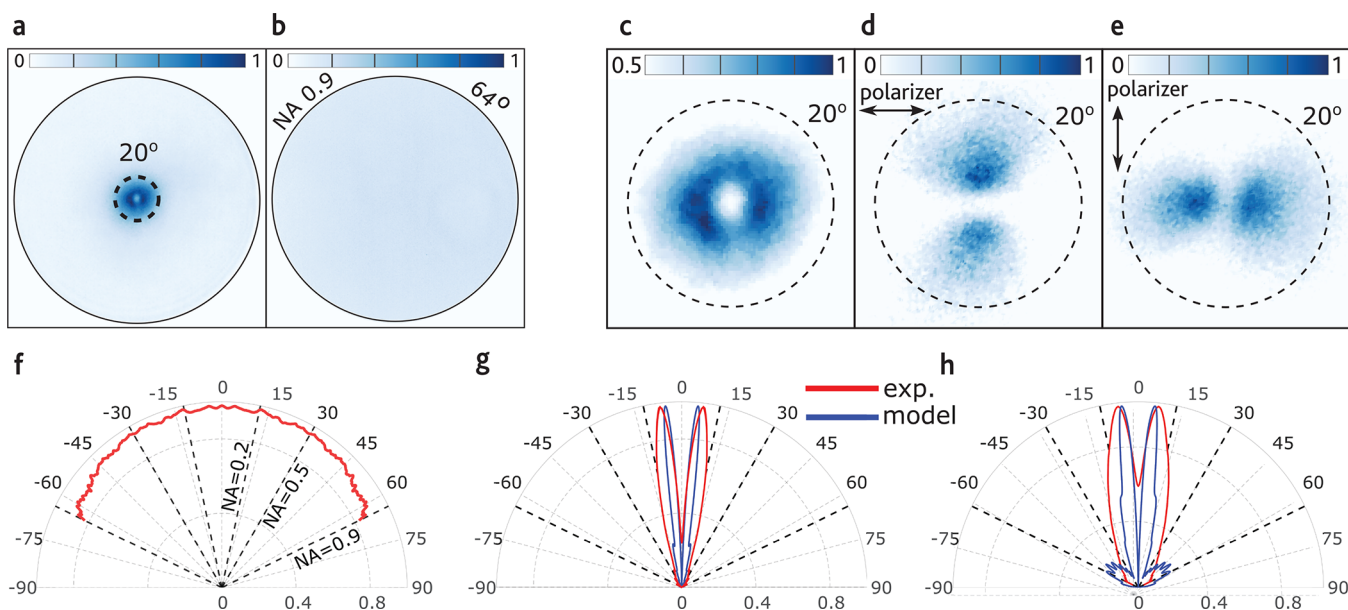


Figure 5. Far-field intensity distributions of NV-ND emission before (b) and after (a,c) coupling to a bull's-eye grating. Solid black circle indicates the limit of the field-of-view, corresponding to the NA = 0.9 of the objective (64°). (c–e) Far-field intensity distribution of coupled NV-ND emission imaged without (c) and with horizontal (d) and vertical (e) analyzers. Images are normalized independently. (f–h) Experimentally measured (red) and modeled (blue) angular distributions of emission intensity of NV-ND before coupling (f) and coupled to plasmonic grating for (g) emission filtered at 680 ± 5 nm and (h) broad spectral range.

$\tau_{average} = (A_1\tau_1^2 + A_2\tau_2^2)/(A_1\tau_1 + A_2\tau_2)$, as we measured the multiexponential decay lifetime utilizing time correlated single photon counting (TCSPC).⁴⁷ The lifetimes of NV centers in nanodiamonds can vary from ~ 10 to 50 ns.⁴⁸ Also, the lifetime is shortened in the presence of metal nearby NV-ND. Our NV-ND is placed on top of the Ag film which can explain a short ~ 10 ns lifetimes measured.

To check the quality of the radially polarized single-photon emission, we measure the second-order correlation (g^2) presented in Figure 4(d,e). The chosen NV-ND shows a $g^2(0) = 0.24$, well below 0.5, indicating a single-photon emitter. After fabricating the bull's-eye antenna, we note an increase of $g^2(0)$ to 0.49. This residual correlation count around $\tau = 0$ s can arise from the weak excitation of trace amounts of HSQ or silver oxide molecules around NV-ND.

The saturation curves are presented in Figure 4(b). We observe a 3-fold enhancement of saturated counts after coupling to the plasmonic environment. The collected count rate increases from $I_{sat}(\text{uncoupled}) = 150$ Kcps to $I_{sat}(\text{coupled}) = 440$ Kcps. The saturation laser power changes from $P_{sat}(\text{uncoupled}) = 0.6$ mW to $P_{sat}(\text{coupled}) = 1.1$ mW. Taking into account $\tau_{uc}/\tau_c = 1.4$ times shortening of the emission lifetime, we assume that an increase of the photon rate after coupling to the plasmonic structure originates from the efficient redirection of energy of SPP waves to the free space in the shape of the collimated radially polarized beam. The fitting model is given by equation $I = I_{sat}[P/(P + P_{sat})]$.

The redistribution of far-field intensity is shown in Figure 5(a),(b). Homogeneous intensity distribution from uncoupled NV-ND transforms to a well-collimated radially polarized beam with emission peaked at $\theta_{max} = 7^\circ$ and 11° divergence. Divergence is defined as a half-width half-maximum of the single emission lobe in the 2D projection of angular distribution. The radial polarization of the outcoupled beam is confirmed by measurements with a polarization analyzer in the optical path and is shown in Figure 5(e),(f).

The angular emission patterns measured with a filter at 680 nm with an fwhm of ~ 10 nm and for the broad emission spectrum are presented in Figure 5(c) and (g), respectively. Spectral filtration results in reducing beam divergence to 6° from 11° . Angular distribution of NV-ND emission before coupling to bull's-eye grating is shown in Figure 5(f). The experimentally measured beam is more divergent than simulated because of the fabrication imperfections. A large part of the photons is emitted into an NA < 0.2. Therefore, emission can be coupled to the multimode fiber without any additional optics.

The higher CE values can be reached using high refractive index materials for ridges.³⁶ For example, a plasmonic antenna with TiO_2 (refractive index 2.2) ridges allows collecting 95% of emission with 0.9 NA objective and 70% with 0.2 NA objective (SI, Figure S9). The dominant reason for the CE increase is enhancing the Purcell effect and the respective growth of the emission rate. Also, fewer structure periods are needed to outcouple the SPP energy if using high refractive index ridges. The reduced structure size corresponds to the smaller SPP propagation distance and, consequently, smaller ohmic losses. We deposited HSQ ridges because of our fabrication possibilities.

Despite the high CE, the beam divergence is higher for the TiO_2 structure than for the HSQ structure. The TiO_2 structure has a smaller effective emission area or, in other words, a smaller beam waist which causes higher beam divergence. For example, for optimized HSQ and TiO_2 structures, corresponding emission peaks appear at 5° and 8° correspondingly (SI, Figure S9).

In conclusion, the proposed methodology allows for an increase in the collected number of photons by 3 times and obtain a well-collimated radially polarized single-photon beam, with emission peak radiated at 7° with 11° divergence. Using such a hybrid plasmonic device is a promising route for efficient directional radially polarized single-photon sources

requiring only very simple, cheap, and compact low-NA optics. Furthermore, for emitters with narrow emission such as germanium vacancy (GeV) centers in diamonds, these gratings can be combined with Bragg gratings to obtain Purcell enhancement together with high collection efficiency and radial polarization of photons.

■ ASSOCIATED CONTENT

SI Supporting Information

The Supporting Information is available free of charge at <https://pubs.acs.org/doi/10.1021/acsp Photonics.1c00459>.

S1: experiment, S2: numerical simulations (PDF)

■ AUTHOR INFORMATION

Corresponding Author

Danylo Komisar – Center for Nano Optics, University of Southern Denmark, DK-5230 Odense M, Denmark;

orcid.org/0000-0001-8856-7586; Email: dak@mci.sdu.dk

Authors

Shailesh Kumar – Center for Nano Optics, University of Southern Denmark, DK-5230 Odense M, Denmark;

orcid.org/0000-0001-5795-0910

Yinhui Kan – Center for Nano Optics, University of Southern Denmark, DK-5230 Odense M, Denmark; College of Astronautics, Nanjing University of Aeronautics and Astronautics, Nanjing 210016, China

Cuo Wu – Center for Nano Optics, University of Southern Denmark, DK-5230 Odense M, Denmark; Institute of Fundamental and Frontier Sciences, University of Electronic Science and Technology of China, Chengdu 610054, China

Sergey I. Bozhevolnyi – Center for Nano Optics, University of Southern Denmark, DK-5230 Odense M, Denmark; Danish Institute for Advanced Study, University of Southern Denmark, DK-5230 Odense M, Denmark; orcid.org/0000-0002-0393-4859

Complete contact information is available at: <https://pubs.acs.org/doi/10.1021/acsp Photonics.1c00459>

Notes

The authors declare no competing financial interest.

■ ACKNOWLEDGMENTS

The authors acknowledge financial support from VILLUM FONDEN by a research grant (35950) and the Villum Kann Rasmussen Foundation (Award in Technical and Natural Sciences 2019).

■ REFERENCES

- (1) Dorn, R.; Quabis, S.; Leuchs, G. Sharper Focus for a Radially Polarized Light Beam. *Phys. Rev. Lett.* **2003**, *91*, 233901.
- (2) Kozawa, Y.; Matsunaga, D.; Sato, S. Superresolution imaging via superoscillation focusing of a radially polarized beam. *Optica* **2018**, *5*, 86–92.
- (3) Miao, P.; Zhang, Z.; Sun, J.; Walasik, W.; Longhi, S.; Litchinitser, N. M.; Feng, L. Orbital angular momentum microlaser. *Science* **2016**, *353*, 464–467.
- (4) Wu, G.; Wang, F.; Cai, Y. Generation and self-healing of a radially polarized Bessel-Gauss beam. *Phys. Rev. A: At., Mol., Opt. Phys.* **2014**, *89*, 043807.
- (5) Nape, I.; Otte, E.; Vallés, A.; Rosales-Guzmán, C.; Cardano, F.; Denz, C.; Forbes, A. Self-healing high-dimensional quantum key

distribution using hybrid spin-orbit Bessel states. *Opt. Express* **2018**, *26*, 26946–26960.

(6) Rosales-Guzmán, C.; Ndagano, B.; Forbes, A. A review of complex vector light fields and their applications. *J. Opt.* **2018**, *20*, 123001.

(7) O'Brien, J. L. Optical Quantum Computing. *Science* **2007**, *318*, 1567–1570.

(8) Kimble, H. J. The quantum internet. *Nature* **2008**, *453*, 1023–1030.

(9) Slussarenko, S.; Pryde, G. J. Photonic quantum information processing: A concise review. *Appl. Phys. Rev.* **2019**, *6*, 041303.

(10) Pirandola, S.; Bardhan, B. R.; Gehring, T.; Weedbrook, C.; Lloyd, S. Advances in photonic quantum sensing. *Nat. Photonics* **2018**, *12*, 724–733.

(11) Berchera, I. R.; Degiovanni, I. P. Quantum imaging with sub-Poissonian light: challenges and perspectives in optical metrology. *Metrologia* **2019**, *56*, 024001.

(12) Wang, J.; Sciarino, F.; Laing, A.; Thompson, M. G. Integrated photonic quantum technologies. *Nat. Photonics* **2020**, *14*, 273–284.

(13) Higginbottom, D. B.; Slodicka, L.; Aranedá, G.; Lachman, L.; Filip, R.; Hennrich, M.; Blatt, R. Pure single photons from a trapped atom source. *New J. Phys.* **2016**, *18*, 093038.

(14) Nicolet, A. A. L.; Hofmann, C.; Kol'chenko, M. A.; Kozankiewicz, B.; Orrit, M. Single Dibenzoterylene Molecules in an Anthracene Crystal: Spectroscopy and Photophysics. *ChemPhysChem* **2007**, *8*, 1215–1220.

(15) Huang, H.; Manna, S.; Schimpf, C.; Reindl, M.; Yuan, X.; Zhang, Y.; da Silva, S. F. C.; Rastelli, A. Bright Single Photon Emission from Quantum Dots Embedded in a Broadband Planar Optical Antenna. *Adv. Opt. Mater.* **2021**, *9*, 2001490.

(16) Aharonovich, I.; Englund, D.; Toth, M. Solid-state single-photon emitters. *Nat. Photonics* **2016**, *10*, 631–641.

(17) Jelezko, F.; Wrachtrup, J. Single defect centres in diamond: A review. *Phys. Status Solidi A* **2006**, *203*, 3207–3225.

(18) Schirhagl, R.; Chang, K.; Loretz, M.; Degen, C. L. Nitrogen-Vacancy Centers in Diamond: Nanoscale Sensors for Physics and Biology. *Annu. Rev. Phys. Chem.* **2014**, *65*, 83–105.

(19) Kolesov, R.; Grotz, B.; Balasubramanian, G.; Stöhr, R. J.; Nicolet, A. A. L.; Hemmer, P. R.; Jelezko, F.; Wrachtrup, J. Wave-particle duality of single surface plasmon polaritons. *Nat. Phys.* **2009**, *5*, 470–474.

(20) Schietinger, S.; Barth, M.; Aichele, T.; Benson, O. Plasmon-Enhanced Single Photon Emission from a Nanoassembled Metal-Diamond Hybrid Structure at Room Temperature. *Nano Lett.* **2009**, *9*, 1694–1698.

(21) Faraon, A.; Barclay, P. E.; Santori, C.; Fu, K.-M. C.; Beausoleil, R. G. Resonant enhancement of the zero-phonon emission from a colour centre in a diamond cavity. *Nat. Photonics* **2011**, *5*, 301–305.

(22) Huck, A.; Kumar, S.; Shakoor, A.; Andersen, U. L. Controlled Coupling of a Single Nitrogen-Vacancy Center to a Silver Nanowire. *Phys. Rev. Lett.* **2011**, *106*, 096801.

(23) Kumar, S.; Huck, A.; Andersen, U. L. Efficient Coupling of a Single Diamond Color Center to Propagating Plasmonic Gap Modes. *Nano Lett.* **2013**, *13*, 1221–1225.

(24) Kumar, S.; Huck, A.; Chen, Y.; Andersen, U. L. Coupling of a single quantum emitter to end-to-end aligned silver nanowires. *Appl. Phys. Lett.* **2013**, *102*, 103106.

(25) Bermúdez-Ureña, E.; Gonzalez-Ballester, C.; Geiselmann, M.; Marty, R.; Radko, I. P.; Holmgaard, T.; Alaverdyan, Y.; Moreno, E.; Garcia-Vidal, F. J.; Bozhevolnyi, S. I.; Quidant, R. Coupling of individual quantum emitters to channel plasmons. *Nat. Commun.* **2015**, *6*, 7883.

(26) Siampour, H.; Kumar, S.; Bozhevolnyi, S. I. Nanofabrication of Plasmonic Circuits Containing Single Photon Sources. *ACS Photonics* **2017**, *4*, 1879–1884.

(27) Andersen, S. K. H.; Kumar, S.; Bozhevolnyi, S. I. Ultrabright Linearly Polarized Photon Generation from a Nitrogen Vacancy Center in a Nanocube Dimer Antenna. *Nano Lett.* **2017**, *17*, 3889–3895.

(28) Siampour, H.; Kumar, S.; Bozhevolnyi, S. I. Chip-integrated plasmonic cavity-enhanced single nitrogen-vacancy center emission. *Nanoscale* **2017**, *9*, 17902–17908.

(29) Kumar, S.; Andersen, S. K.; Bozhevolnyi, S. I. Extremely confined gap-plasmon waveguide modes excited by nitrogen vacancy centers in diamonds. *ACS Photonics* **2019**, *6*, 23–29.

(30) Bogdanov, S. I.; Shalaginov, M. Y.; Lagutchev, A. S.; Chiang, C.-C.; Shah, D.; Baburin, A. S.; Ryzhikov, I. A.; Rodionov, I. A.; Kildishev, A. V.; Boltasseva, A.; Shalae, V. M. Ultrabright Room-Temperature Sub-Nanosecond Emission from Single Nitrogen-Vacancy Centers Coupled to Nanopatch Antennas. *Nano Lett.* **2018**, *18*, 4837–4844.

(31) Bozhevolnyi, S. I.; Khurgin, J. B. Fundamental limitations in spontaneous emission rate of single-photon sources. *Optica* **2016**, *3*, 1418–1421.

(32) Fernández-Domínguez, A. I.; Bozhevolnyi, S. I.; Mortensen, N. A. Plasmon-Enhanced Generation of Nonclassical Light. *ACS Photonics* **2018**, *5*, 3447–3451.

(33) Kumar, S.; Bozhevolnyi, S. I. Excitation of Hybrid Plasmonic Waveguide Modes by Colloidal Quantum Dots. *ACS Photonics* **2019**, *6*, 1587–1593.

(34) Kumar, S.; Leißner, T.; Boroviks, S.; Andersen, S. K. H.; Fiutowski, J.; Rubahn, H.-G.; Mortensen, N. A.; Bozhevolnyi, S. I. Efficient Coupling of Single Organic Molecules to Channel Plasmon Polaritons Supported by V-Grooves in Monocrystalline Gold. *ACS Photonics* **2020**, *7*, 2211–2218.

(35) Kan, Y.; Andersen, S. K. H.; Ding, F.; Kumar, S.; Zhao, C.; Bozhevolnyi, S. I. Metasurface-Enabled Generation of Circularly Polarized Single Photons. *Adv. Mater.* **2020**, *32*, 1907832.

(36) Andersen, S. K. H.; Bogdanov, S.; Makarova, O.; Xuan, Y.; Shalaginov, M. Y.; Boltasseva, A.; Bozhevolnyi, S. I.; Shalae, V. M. Hybrid Plasmonic Bullseye Antennas for Efficient Photon Collection. *ACS Photonics* **2018**, *5*, 692–698.

(37) Kan, Y.; Kumar, S.; Ding, F.; Zhao, C.; Bozhevolnyi, S. I. Spin-Orbit Controlled Excitation of Quantum Emitters in Hybrid Plasmonic Nanocircuits. *Adv. Opt. Mater.* **2020**, *8*, 2000854.

(38) Kumar, S.; Wu, C.; Komisar, D.; Kan, Y.; Kulikova, L. F.; Davydov, V. A.; Agafonov, V. N.; Bozhevolnyi, S. I. Fluorescence enhancement of a single germanium vacancy center in a nanodiamond by a plasmonic Bragg cavity. *J. Chem. Phys.* **2021**, *154*, 044303.

(39) Johnson, P. B.; Christy, R. W. Optical Constants of the Noble Metals. *Phys. Rev. B* **1972**, *6*, 4370–4379.

(40) Malitson, I. H. Interspecimen Comparison of the Refractive Index of Fused Silica. *J. Opt. Soc. Am.* **1965**, *55*, 1205–1209.

(41) Palik, E.; Ghosh, G.; Jovanovich, H. B.; Firm, K.; Lowrie, W. *Handbook of Optical Constants of Solids*; Academic Press handbook series v. 1; Academic Press: 1985; DOI: 10.1016/C2009-0-20920-2.

(42) Epstein, R. J.; Mendoza, F. M.; Kato, Y. K.; Awschalom, D. D. Anisotropic interactions of a single spin and dark-spin spectroscopy in diamond. *Nat. Phys.* **2005**, *1*, 94–98.

(43) Dolan, P. R.; Li, X.; Storteboom, J.; Gu, M. Complete determination of the orientation of NV centers with radially polarized beams. *Opt. Express* **2014**, *22*, 4379–4387.

(44) Drexhage, K. Influence of a dielectric interface on fluorescence decay time. *J. Lumin.* **1970**, *1–2*, 693–701.

(45) Ford, G.; Weber, W. Electromagnetic interactions of molecules with metal surfaces. *Phys. Rep.* **1984**, *113*, 195–287.

(46) Chance, R. R.; Miller, A. H.; Prock, A.; Silbey, R. Fluorescence and energy transfer near interfaces: The complete and quantitative description of the Eu³⁺ mirror systems. *J. Chem. Phys.* **1975**, *63*, 1589–1595.

(47) Zatyrb, G.; Klak, M. M. On the choice of proper average lifetime formula for an ensemble of emitters showing non-single exponential photoluminescence decay. *J. Phys.: Condens. Matter* **2020**, *32*, 415902.

(48) Storteboom, J.; Dolan, P.; Castelletto, S.; Li, X.; Gu, M. Lifetime investigation of single nitrogen vacancy centres in nanodiamonds. *Opt. Express* **2015**, *23*, 11327–11333.

Supporting Information:

Generation of radially polarized single photons with plasmonic bullseye antennas

Danylo Komisar,^{*,†} Shailesh Kumar,[†] Yinhui Kan,^{†,‡} Cuo Wu,[†] and Sergey I.
Bozhevolnyi^{†,§}

[†]*Center for Nano Optics, University of Southern Denmark, DK-5230 Odense M, Denmark*

[‡]*College of Astronautics, Nanjing University of Aeronautics and Astronautics, Nanjing
210016, China*

[¶]*Institute of Fundamental and Frontier Sciences, University of Electronic Science and
Technology of China, Chengdu, 610054 P. R. China*

[§]*Danish Institute for Advanced Study, University of Southern Denmark, Campusvej 55,
DK-5230 Odense M, Denmark*

E-mail: dak@mci.sdu.dk

Contents

| | |
|--|-------------|
| S1 Experiment | S-3 |
| S1.1 Optical set-up | S-3 |
| S1.2 Sample fabrication | S-6 |
| S2 Numerical modelling | S-8 |
| S2.1 Inner radius optimization | S-10 |
| S2.2 Number of ridges optimization | S-11 |
| S2.3 Optical properties of substrate | S-12 |
| S2.4 Resonant SPP outcoupling | S-14 |
| S2.5 TiO ₂ structure optimization | S-16 |
| References | S-17 |

S1 Experiment

S1.1 Optical set-up

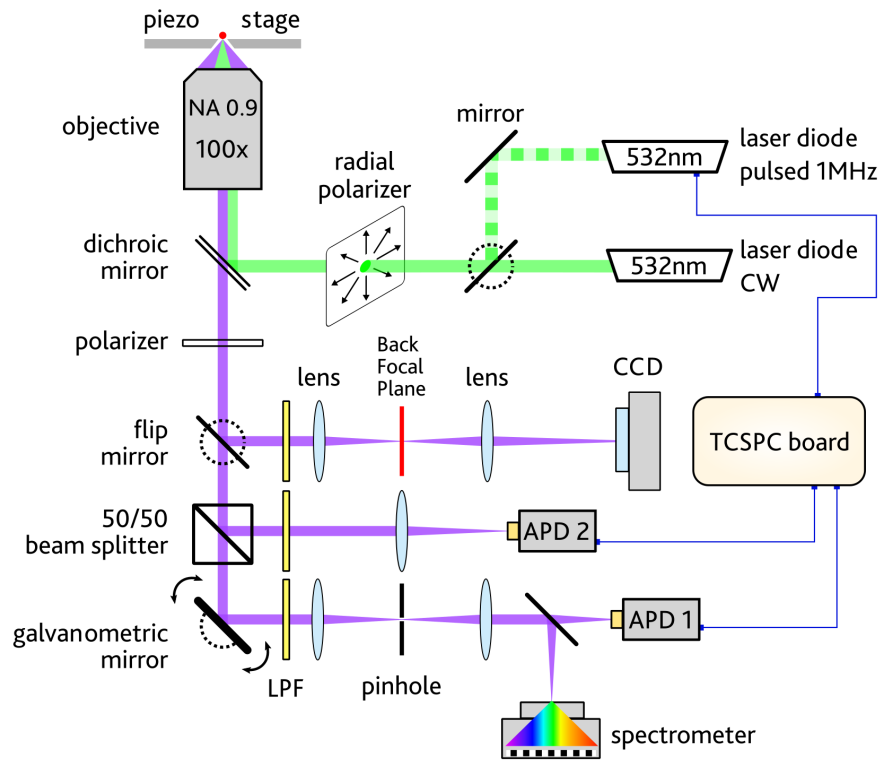


Figure S1: Schematic of experimental setup. CCD — camera. APD — Avalanche Photodiode TCSPC — Time Correlated Single Photon Counting board. LPF - 550 nm long pass filter.

An experimental set-up schematic is presented in Figure S1. A linearly polarized 532 nm continuous wave (CW) or pulsed laser beam is passed through ARCoOptix RPC Radial Polarization Converter. The Olympus MPLFLN x100 objective with NA=0.9 focuses the radially polarized laser beam on a sample surface. As a result, nanodiamonds containing nitrogen-vacancy centers (NV-ND) in the focal spot are excited by a strong field component normal to the surface. Fluorescence scans are performed by a synchronous movement of piezo-stage with mounted sample and projecting the collected fluorescence emission on the APD through the $75\mu\text{m}$ pinhole. Laser light is filtered out by a set of Semrock FF535-SDi01/FF552-Di02

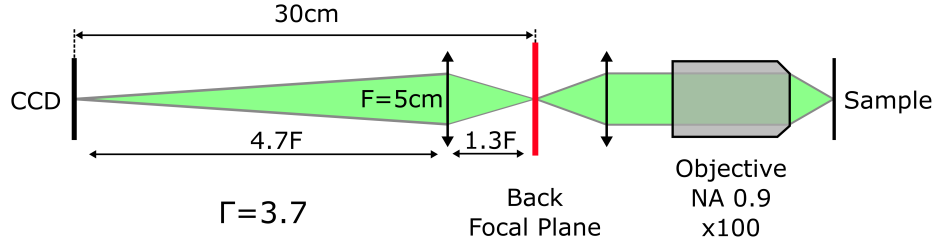


Figure S2: Schematic of back-focal plane (BFP) imaging setup. Γ — magnification factor.

dichroic mirrors and Thorlabs FELH0550 550 nm long-pass filters. Fluorescence spectra are measured using the Andor Ultra 888 USB3–BV spectrometer operating within 540–820 nm. Fluorescence decay-rate and auto-correlation function measurements are carried out using a PicoHarp 300 time-correlated single-photon counting module. A pulsed Pico Quant LDH-P-FA-530L laser is used for pulsed laser excitations. Pulsed laser, together with a PicoQuant τ -SPAD APD, is used for decay-rate measurements. CW excitation and two APDs were utilized for auto-correlation measurements, as shown in Figure S1. The saturation curves of the ND-NV emission are measured by the accumulation of counts from both APDs with excitation laser power ranging from 10 μ W to 3 mW. The back focal plane images are obtained with a Hamamatsu Orca LT+ CCD camera utilizing the optical scheme presented in Figure S3. The Thorlabs LPVIS100-MP2 polarizer is inserted on the optical path for measurement of NV-ND emission polarization properties. Spectrally filtered images are taken with a 680 ± 10 nm bandpass filter in front of the CCD. The SEM images are taken with a 30-kV JEOL-6490 electron microscope. The AFM imaging is performed at the NT-MDT NTEGRA atomic force microscope. All experiments are performed at standard conditions. Degradation of the optical properties was not observed during the experiments.

S1.2 Sample fabrication

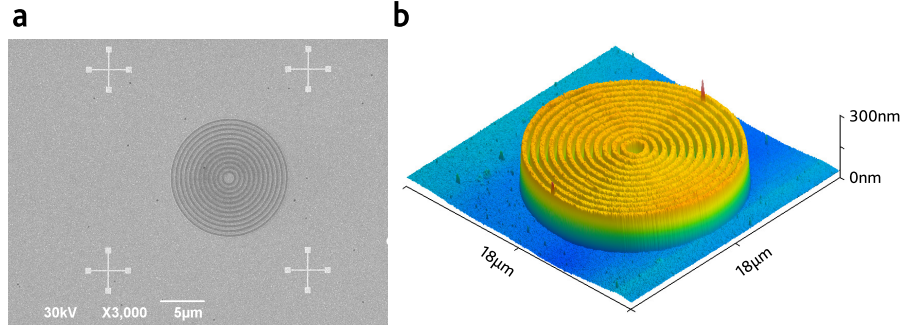


Figure S3: Fabricated device. (a) SEM image of the HSQ bullseye structure with alignment golden markers in corners of the $27 \times 27 \mu\text{m}^2$ area. (b) AFM image of the antenna.

We fabricate samples in four steps:

1. Substrate preparation: A polished Si wafer is coated by thermal evaporation of 3 nm Ti followed by 150 nm Ag, and another 3 nm Ti. Radio frequency (RF) magnetron sputtering of 20 nm SiO_2 layer was done to protect silver from oxidation. Ti layer is used for better adhesion of Si and SiO_2 to metal. Deposition rates for Ti/Ag/Ti/ SiO_2 structure are 0.1/1/0.1/1.5 Å/s subsequently. Chamber pressure is $5 \cdot 10^{-6}$ mbar.
2. Gold markers fabrication by EBL (Electron Beam Lithography): PMMA A2 positive resist is spin-coated at 1580 rpm for 45 sec and baked at 180°C on a hot plate for 2 min to form a ≈ 100 nm layer. $5 \times 5 \mu\text{m}$ golden crosses are patterned on EBL system and developed for 45 sec in 1:3 MIBK:IPA (Methyl isobutyl ketone:Isopropyl alcohol) and rinsed in IPA for 60 sec. Ti(3nm)/Au(35nm) layers are thermally deposited in a vacuum chamber with deposition rates 0.1/1 Å/s and pressure $5 \cdot 10^{-6}$ mbar. The unexposed PMMA is dissolved in acetone during 12 hours lift-off procedure. Samples are ultrasonicated in acetone for 1 min and washed with IPA and DI water. Gold is used as material for markers because it is chemically stable and provides sufficient contrast for optical microscopy and fluorescent mapping.

3. Nanodiamonds deposition: A solution of NV-NDs (Microdiamant) with maximum size ~ 100 nm size is spin-coated on the samples. The positions of diamonds are determined relative to the gold markers from the fluorescent maps. The positioning accuracy is ≈ 50 nm. The positioning procedure is described in previous work^{S1}.
4. Hydrogen silsesquioxane (HSQ) structure fabrication: Negative resist HSQ (Applied Quantum Materials, Canada, 8% solution in MIBK) is spin-coated at 1250 RPM 60 sec and baked at 160°C on a hot plate for 2 min to form a ≈ 180 nm layer. Bullseye antenna structures are patterned around NV-NDs by EBL and developed in 25% TMAH (Tetramethylammonium hydroxide) for 4 min. Samples are rinsed for 1 min with DI water.

The SEM and AFM images of fabricated structure are presented in Figure S4. The optimized bullseye antenna parameters: period $\Lambda=516$ nm, duty cycle $\chi=0.61$, first ridge radius $R_0=520$ nm, ridge width $W=313$ nm, ridge height 180 nm.

S2 Numerical modelling

Numerical simulations are performed in COMSOL Multiphysics 5.4. The proposed design of the plasmonic antenna has rotational symmetry around Z-axis, and we used 2D axisymmetric geometry to reduce the computation time. Solving a 2D slice is enough to obtain 3D field distribution. The calculations are done at an operational wavelength $\lambda_0 = 670$ nm as a central wavelength of the NV-ND emission spectral band. The NV-ND is modelled as a vertically oriented electric dipole. In the “2D axisymmetric” model in COMSOL, boundary conditions prohibit placing the electric dipole directly on the symmetry axis. This obstacle is overcome by introducing a “Magnetic current” element, positioned several nanometers away from the Z symmetry axis. In our case, the distance is 1nm. The resulting electromagnetic field simulates the field of the electric dipole positioned at the R=0 point.

The electric dipole is positioned 50 nm above the 20 nm thick SiO₂ spacer layer. An optically thick layer of metal, i.e. Ag thickness, is chosen to be 100 nm. The maximal mesh grid size is 67 nm for air and 20 nm for HSQ and SiO₂ layers. The grid size in metal varies from 0.5 nm to 5 nm from top to bottom.

The far-field angular distributions are calculated as the distribution of a normal component of a Poynting vector on the arc framing the circular domain with radius $50 \mu m$ in the 2D axisymmetric model. The size of domain is chosen according to the far-field criteria $\sin(\theta) = N_{eff} - \frac{\lambda_0}{L}$ where D - size of scatterer, L - distance to the scatterer, λ_0 - emission wavelength. The circle with a radius of $50 \mu m$ is big enough to let all near field components die. The use of built-in COMSOL near-to-far field transformation to calculate angular distributions is avoided because it provides consistent results only for uniform domain fully enclosing the scatterer. This condition can not be satisfied as far as a metal substrate is included in the calculation domain.

Collection efficiency is calculated as a ratio between total power integrated over NA=0.9/0.5/0.2 and the total power generated by a dipole in the presence of a bullseye structure. The radius of the integration sphere is the same — $50 \mu m$.

We optimized the bullseye structure step by step. The ridge height of 180 nm and SiO₂ thickness of 20 nm is not changed in the optimization process. First, we look for the maximum in CE varying the structure period Λ and duty cycle χ simultaneously. After we found the maximal point, we optimized the inner radius R_0 while other parameters are fixed. Then we check the angular distribution of the far-field emission. Finally, we find a sufficient number of ridges for efficient out-coupling.

The orientation of dipole above the silver film with respect to the surface normal was studied before^{S2}. The most efficient coupling to the SPP mode happens when the dipole is oriented normal to the metal surface, and the separation from the metal is at least 20 nm. The increase of separation distance over 80 nm leads to mitigation of dipole interaction with metal and SPP excitation. The decrease of separation distance to <20 nm results in a significant increase in metal losses. The trade-off for dipole separation lies in between 15 and 80nm. The average radius of the nanodiamonds in the experiment is 50 nm, so we used 50 nm separation from the SiO₂ surface (70 nm from Ag) in the calculation. Optical constants for silver, SiO₂ are taken from^{S3} and^{S4}, correspondingly. The refractive index of HSQ is set to be $n(\text{HSQ})=1.41$, extinction coefficient $k=0$ ^{S5}.

S2.1 Inner radius optimization

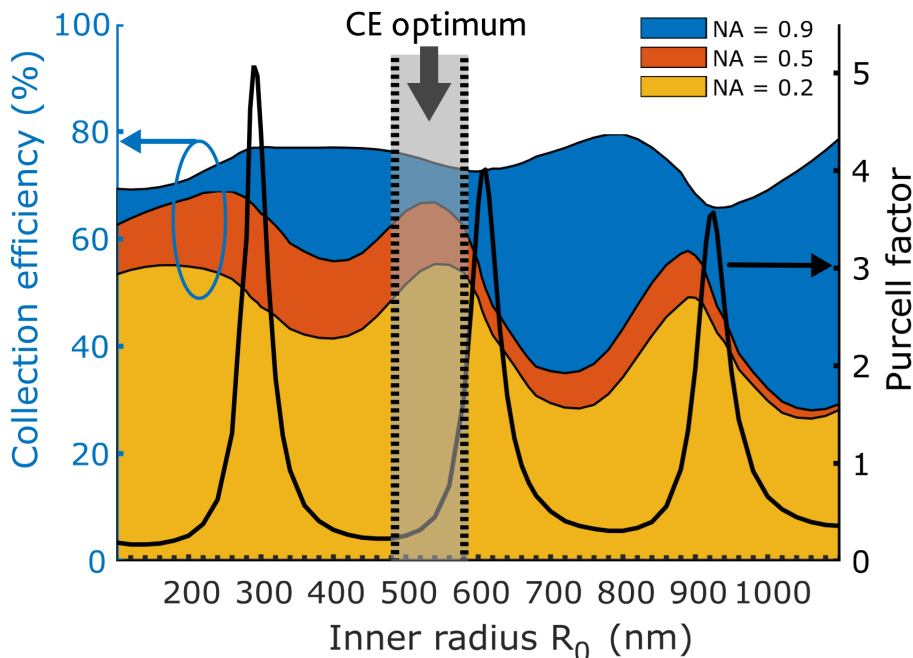


Figure S4: Optimization of the inner radius R_0 of the bullseye antenna. $\Lambda=516$ nm and $\chi=0.61$ are fixed. Collection efficiency maximum for $NA=0.2$ is depicted by the shaded region of optimal R_0 values within spectrum of NV-ND. The optimal inner radius is $R_0=520$ nm. Average Purcell factor value in shaded region is ≈ 1 . Parameters of optimal structure: $R_0=520$ nm, $\Lambda=516$ nm, $W=315$ nm.

SPP reflection from the structure can enhance or diminish the field around the dipole, bringing up or down the dipole emission rate. The first ridge is positioned to match the constructive interference between generated and reflected SPP fields in the antenna center, $R=0$. The R_0 optimum corresponding to the common maximum CE for collection with different $NA=0.5$ objective is depicted in Figure S5 as a range of values because the emission spectrum of the NV-ND emission is wide (spectrum FWHM ≈ 100 nm). The average optimal $R_0=520$ nm was chosen for our experiment. The average Purcell factor value in the marked region ≈ 1 . Purcell factor is defined as a ratio of total power generated by coupled emitter coupled to the total power generated by an uncoupled emitter on the substrate.

S2.2 Number of ridges optimization

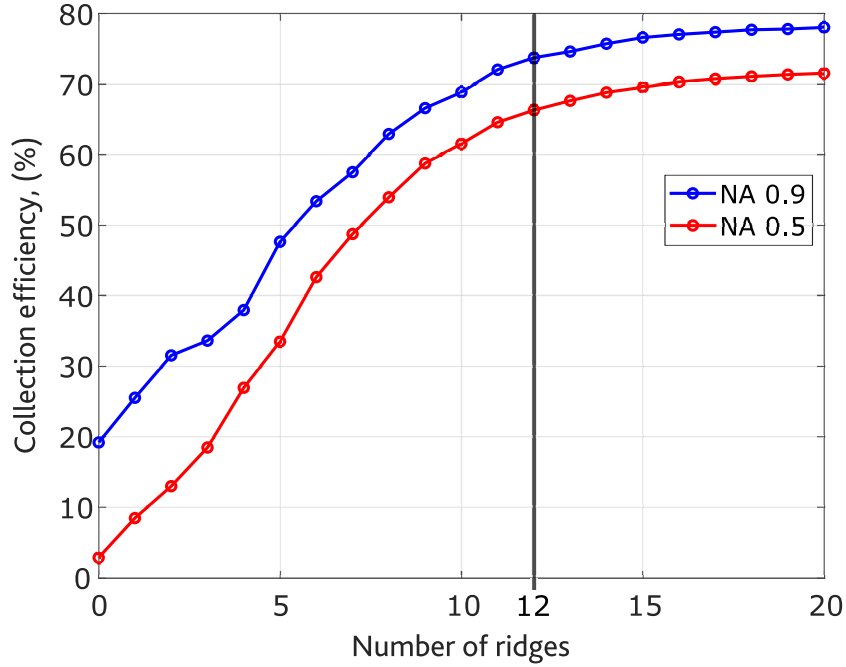


Figure S5: Collection efficiency saturation with increase of number of HSQ ridges building up bullseye structure. 12 ridges is enough to reach 90% of saturated CE (20 ridges).

The optimization of the number of circular ridges of bullseye outcoupling antenna is shown in figure S6. The increase in the number of nano-ridges is reasonable only until some threshold. The threshold was chosen to be 90% of saturated CE value, which corresponds to ~ 12 ridges structure.

S2.3 Optical properties of substrate

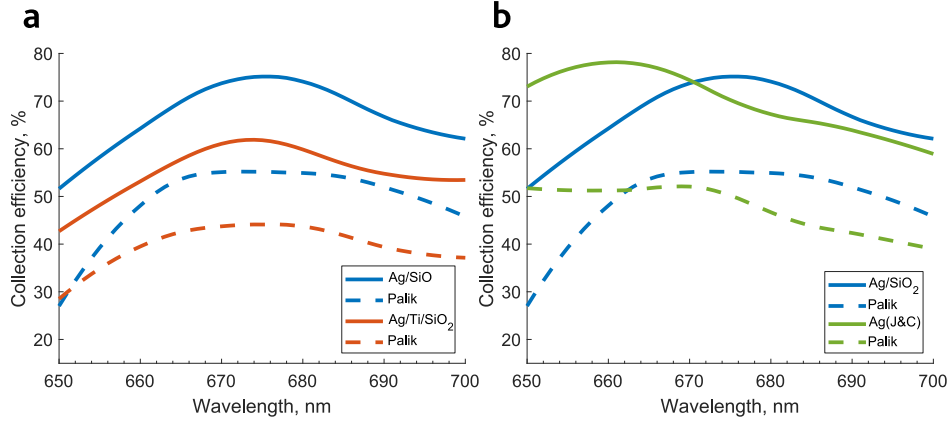


Figure S6: Collection efficiency dependence over operational wavelength modeled for different substrate properties. (a) Addition of 3nm Ti layer (orange) decrease absolute value of CE. (b) Removing of SiO₂ layer from the Ag surface shifts the position of CE maxima. All dependances are calculated for Palik Ag optical constants (dashed) and Johnson&Christy (solid) constants. Palik data shows lower CE because of higher absorption coefficient.

In the experiment, we deposited a 3 nm adhesive Ti layer between Ag and SiO₂. So we checked how the addition of the Ti layer to the computational model affected the results. Collection efficiency relation on wavelength within 650-700 nm is shown in Figure S7(a). The addition of the Ti layer does not shift the CE maximum position and only mitigate the absolute value of CE because of the significant absorption coefficient of Ti. So, the optimization procedure can be done successfully without introducing the Ti layer to the computational model.

We also used a different set of optical constants for our numerical simulation. Comparison of CE calculated for two Ag optical constants sets Johnson&Christy^{S3} and Palik^{S5} is depicted in Figure S7 by solid and dashed lines, respectively. The change of Ag optical constants from Johnson&Christy to Palik also does not change the position of CE maximum because refractive index values are very close for both sets. We see a decrease in the absolute CE value because the absorption coefficient is higher in the Palik data.

Finally, we wanted to check the device performance if the bare silver substrate was

used. The resonance shift to the longer wavelength for bare silver substrate can be seen in Figure S7(b). So, if one wants to optimize antenna parameters on a bare silver substrate, the optimization procedure should be repeated from the very beginning. The 20 nm SiO_2 layer has a significant influence on the wavelength at which the grating scatters efficiently.

S2.4 Resonant SPP outcoupling

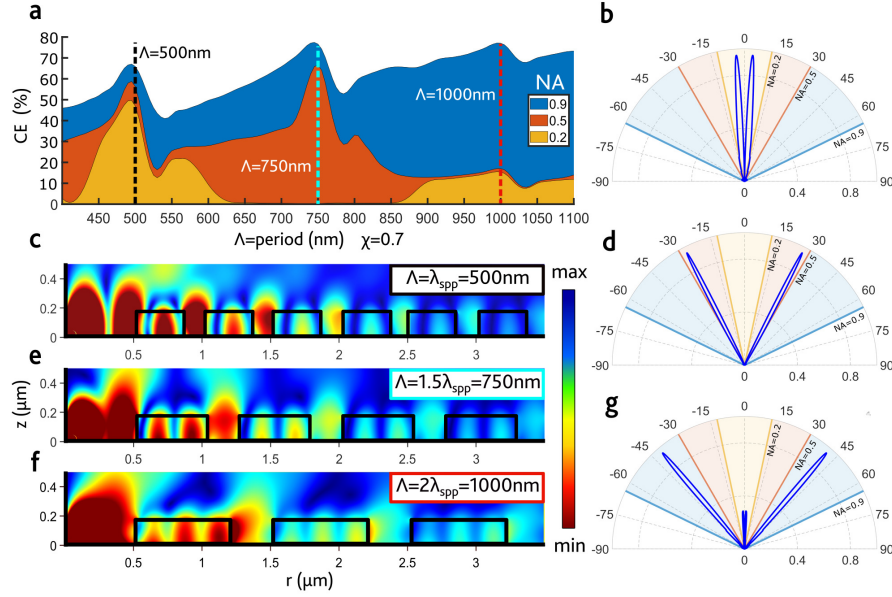


Figure S7: Resonant SPP outcoupling. (a) Collection efficiency of bullseye antenna with duty cycle $\chi=0.7$ over ridges period calculated for NA=0.2/0.5/0.9. (c,e,f) Radial component $|E_r|$ of the near field depicting periodical SPP waves for $n=2,3,4$ Bragg resonances and corresponding normalized far-field angular distributions of outcoupled emission(b,d,g).

In Figure S8(a), we present CE for the fixed duty cycle as the period is changed. Figure S8(c) (e) and (f) show the collection efficiency, near-field distributions for periods (Λ) of 500 nm, 750 nm, and 1000 nm, respectively. Figure S8(b) (d) and (g) show far-field emission patterns for periods (Λ) of 500 nm, 750 nm, and 1000 nm, respectively. Corresponding λ_{spp} for the grating structure is ≈ 500 nm. In the resonance, SPP field distribution repeats itself each structure period. The angle of the maximum emission increases as the structure period Λ increase.

The outcoupled NV-ND emission propagating at several angles simultaneously is illustrated in figure S9(b,c). The modeled emission distributions are in accordance with phase-matching condition $k_{spp} = k_0 \cdot \sin(\theta) \pm N \cdot G$, where $G = 2\pi/\Lambda$ is the grating vector, Λ is a structure period, $k_0 = 2\pi/\lambda_0$ is a propagation constant of in-plane wave vector of free radiation, θ is a angle of emission propagation. k_{spp} is a wave vector of SPP.

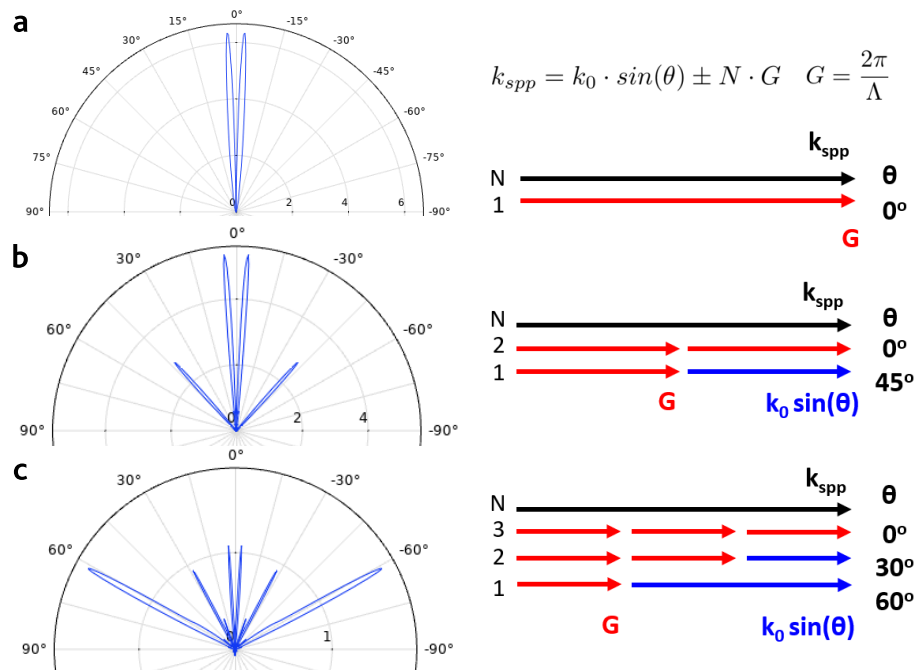


Figure S8: Numerically calculated device emission at one (a), two (b) or three (c) directions. Corresponding structure periods are $\Lambda=550$ nm, 1100 nm and 1650 nm. Duty cycle $\chi=0.6$.

S2.5 TiO₂ structure optimization

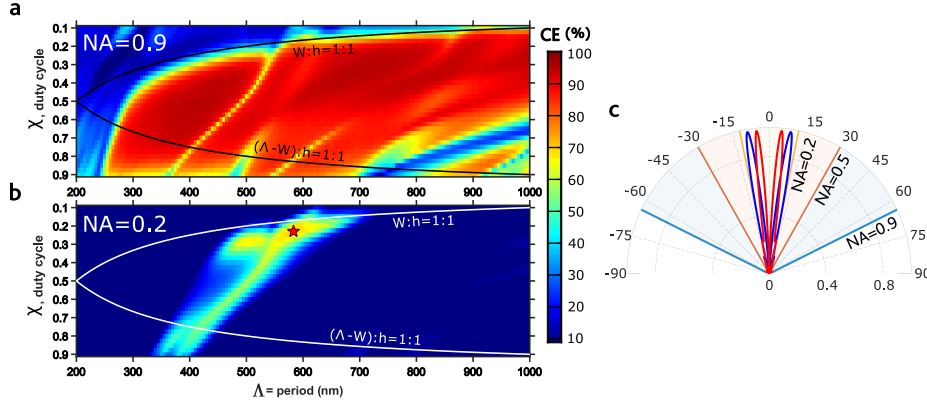


Figure S9: (a) and (b) Maps of collection efficiency over TiO₂ structure period and duty cycle calculated for collection angles 64° (NA=0.9) and 12° (NA=0.2). Red star: $\Lambda=585$ nm, $\chi=0.23$ corresponds to the maximum of CE. The region of (Λ, χ) parameters feasible for e-beam lithography implementation is limited by structure aspect ratio 1:1 and lies between solid lines. The ridge height is 100nm. (c) Far field angular intensity distributions for optimized TiO₂ (blue) and HSQ (red) structures. Corresponding radiation peaks appear at 8 and 5 degrees, respectively.

The CE maps obtained for high and low NA objectives, by varying TiO₂ bullseye structure period and duty cycle are presented in Figure S10(a) and (b), respectively. TiO₂ ridge height is 100 nm. We used structure inner radius $R_0 = 220$ nm in calculations. We optimized it separately. The structure with period $\Lambda = 585$ nm and duty cycle $\chi = 0.225$ has the highest CE= 70% for NA= 0.2 objective. 95% of emitted light can be collected by high NA (0.9) objective. The corresponding set of grating parameters is marked on the map by a red star.

The far-field angular distributions of emission of optimized TiO₂ and HSQ structures is shown in FigureS10(c). The HSQ structure produces a less divergent beam with an emission peak at 5° with TiO₂ peak at 8°. The higher emission angle of the TiO₂ structure corresponds to the smaller beam waist. Put it differently, the effective emission area is smaller for TiO₂ because less grating periods is needed to scatter SPP energy in comparison with the HSQ bullseye antenna with a smaller refractive index. The refractive indexes of HSQ $n(\text{HSQ})=1.41$ and $n(\text{TiO}_2)=2.2$ at $\lambda_0 = 670$ nm were used for modelling.

References

- (S1) Kan, Y.; Andersen, S. K. H.; Ding, F.; Kumar, S.; Zhao, C.; Bozhevolnyi, S. I. Metasurface-Enabled Generation of Circularly Polarized Single Photons. *Advanced Materials* **2020**, *32*, 1907832.
- (S2) Andersen, S. K. H.; Bogdanov, S.; Makarova, O.; Xuan, Y.; Shalaginov, M. Y.; Boltas-seva, A.; Bozhevolnyi, S. I.; Shalaev, V. M. Hybrid Plasmonic Bullseye Antennas for Efficient Photon Collection. *ACS Photonics* **2018**, *5*, 692–698.
- (S3) Johnson, P. B.; Christy, R. W. Optical Constants of the Noble Metals. *Physical Review B* **1972**, *6*, 4370–4379.
- (S4) Malitson, I. H. Interspecimen Comparison of the Refractive Index of Fused Silica. *Journal of the Optical Society of America* **1965**, *55*, 1205.
- (S5) Palik, E.; Ghosh, G.; Jovanovich, H. B.; (Firm), K.; Lowrie, W. *Handbook of Optical Constants of Solids*; Academic Press handbook series v. 1; Academic Press, 1985.